Available online at BCREC website: https://bcrec.id

Bulletin of Chemical Reaction Engineering & Catalysis, 17 (2) 2022, 403-419

Research Article

Nanocomposite ZnO/g-C_3N_4 for Improved Degradation of Dyes under Visible Light: Facile Preparation, Characterization, and Performance Investigations

Tu Anh Nguyen Thi, Anh-Tuan Vu*

School of Chemical Engineering, Hanoi University of Science and Technology, Hanoi, Vietnam.

Received: 24th March 2022; Revised: 12nd May 2022; Accepted: 13rd May 2022
Available online: 14th May 2022; Published regularly: June 2022

Abstract

In this study, ZnO/g-C_3N_4 nanocomposites were prepared via a physical mixing-calcination process for improved degradation of dyes under visible light irradiation. The BET surface area, pore volume, crystal size, and pH_{pzc} of the ZnO/g-C_3N_4 composite were 3.9 m^2/g, 0.034 cm^3/g, 18.1 nm, and 7.7, respectively. Although the morphology of the ZnO/g-C_3N_4 composite was very different from that of pure g-C_3N_4, their average pore sizes were similar. The E_g of the ZnO/g-C_3N_4 composite (3.195 eV) was slightly lower than that of ZnO (3.195) but much higher than that of g-C_3N_4 (2.875). The interface interaction of ZnO and g-C_3N_4, which was revealed by oscillations of Zn-C, benefited the transport of photoinduced charge carriers and reduced the recombination of electron-hole. As the result, the ZnO/g-C_3N_4 composite had higher photocatalytic activity than ZnO and g-C_3N_4. Its degradation efficiency (*DE*) value for methylene blue (MB) in 90 min and rate constant were 93.2 % and 0.025 min^{-1}, respectively. In addition, the effects of ZnO/urea molar ratio, catalyst dosage, solution pH, and concentration of dye on photocatalytic degradation of MB were completely investigated. The photocatalytic performance of the ZnO/g-C_3N_4 composite was evaluated by the degradation of other persistent organic compounds, also compared to other catalysts in the literatures.

Keywords: ZnO; g-C_3N_4; Composite; Photocatalyst; Dye; Visible Light

How to Cite: T.A. Nguyen Thi, A.-T. Vu. (2022). Nanocomposite ZnO/g-C_3N_4 for Improved Degradation of Dyes under Visible Light: Facile Preparation, Characterization, and Performance Investigations. *Bulletin of Chemical Reaction Engineering & Catalysis*, 17(2), 403-419 (doi: 10.9767/bcrec.17.2.13931.403-419)

Permalink/DOI: https://doi.org/10.9767/bcrec.17.2.13931.403-419

1. Introduction

The first synthetic organic dye, mauve, was discovered by William Perkin in 1865. This discovery led to a revolution in the dye industry and initiated the production of synthetic organic dyes on a global scale [1]. Nowadays, dyes are widely used not only in the textile industry but also in the tannery, and printing [2,3], cosmetic [4], food [5], human and veterinary medicine industries [6] and other industries. The annual output of synthetic dyes is up to 1,000,000 tons with 100,000 different types [7]. Besides being used to create commercial products, a large number of dyes is leftover and released into the environment. The dyes are usually stable, and their molecular structure contains azo and aromatic functional groups, chlorine and sulfur elements, they are harmful to humans and aquatic systems if they are not handled thoroughly. Therefore, finding an appropriate, environmentally friendly, and cost-effective method is of great interest to scientists worldwide.

Azo dye class, represented by methylene blue (MB), tartazin (TA), janus green B (JGB), and conggo red (CR), are the most widely used as colorants today, accounting for about 60 % of

---

* Corresponding Author.
Email: tuan.vuanh@hust.edu.vn (A.T. Vu);
Telp: +84-912911902, Fax: +84-02438680070

the world's dye production because they have low cost, high intensity, and colorfastness. However, they also cause extremely negative impacts on the environment, especially the aquatic environment. Azo dyes are less biodegradable, stable to light, and resistant to attack by microorganisms. When azo dye ions enter the aquatic environment, they can combine with suspended organic solid particles to form stable toxic compounds that adhere to the sludge. These toxics get into aquatic animals 's body, through the food chain to humans, causing health disorders, such as hypertension, cramps, nausea, bleeding, ulceration of the skin or the membranes, and mucous membranes. Depending on the content of the dyes, they can cause serious damage to the internal organs, reproductive and nervous systems [8]. Caffeine (CAF), $C_8H_{10}N_4O_2$, an alkaloid belonging to the methylxanthine family, is an example of PPCPs that often appears in surface water. Caffeine is present in beverages, such as coffees, teas, soft drinks, chocolate, and some drugs, which makes it a widely consumed substance in the world. Caffeine alone does not seem to be toxic to domestic organisms. However, the presence of too much of it in surface water, along with other organic pollutants, such as pesticides, pharmaceuticals, and other chemicals, has serious implications for organisms and humans.

To treat dyes from wastewater, many methods have been used like adsorption [9], biological treatment [10], membrane separation [11], ion-exchange [12], ultrafiltration [13], and coagulation/flocculation [14]. However, the advanced oxidation process (AOP) is still the preferable choice, because of the advantages of high efficiency and less secondary pollution. AOPs are oxidative degradation processes based on the active free radical hydroxyl $OH^\bullet$ generated during treatment with a short duration [15]. It is the strongest known oxidizing agent, non-selectively oxidizing all organic compounds, even those that are difficult to mineralize them to non-toxic inorganic compounds, such as CO_2, H_2O, or readily more degradable such as short-chain organic and inorganic acids.

Due to its environment-friendly operation and no by-products, photocatalysts are favored and extensively used materials for advanced oxidation processes. When a photocatalyst absorbs light irradiation for generating charge carriers and shifting from the valence band (*VB*) to the conduction band (*CB*), photodegradation reaction occurs on its active surface through the formation of $OH^\bullet$ and $O_2^{\bullet-}$, which rapidly breakdown target pollutants into the end products of CO_2 and H_2O [16]. Graphitic carbon nitride (g-C_3N_4) is a non-metallic polymer semiconductor, possessing many promising properties that make it a potential photocatalytic material. The g-C_3N_4 material can withstand high temperatures above 600 °C, even in the presence of oxygen [17]. Because of its inertness and stability in many solvents g-C_3N_4, it is expected to give some good results in the catalytic field [18]. In addition, g-C_3N_4 has an average band gap energy of 2.7 eV, equivalent to an adsorbed light wavelength of 460 nm, which makes carbon nitride active in visible light. However, due to the strong occurrence of electron-hole recombination, the photocatalytic activity in the visible light of this material is not high [19,20]. Therefore, studies to improve the photocatalyst efficiency of g-C_3N_4 by modification of crystal size, surface morphology, texture properties, physicochemical parameters would be fascinating research.

Zinc oxide (ZnO) is one of the semiconductors studied and applied in many industries [21]. Many studies show that ZnO is environmentally friendly and able to decompose and mineralize environmental pollutants [21-23]. The biggest advantage of ZnO is the spectral region that it can absorb larger and larger than some other metals. However, ZnO has a wide band gap energy (about 3.37 eV), corresponding to an absorbed wavelength of 369 nm, it is inactive in the visible light. In order to overcome the barriers of bandgap energy and fast recombination of electrons and holes for achieve practical application goals, composite materials need to be developed.

In this study, we focused on the preparation of ZnO/g-C_3N_4 nanocomposites through facile precipitation and physical mixing-calcination for treating dye-containing wastewater under visible light irradiation. The catalytic activity of composite was evaluated by degrading MB in water under visible light irradiation. The effects of ZnO/urea mass ratio, catalyst dosage, concentration of MB, and initial solution pH on photocatalytic degradation of MB were investigated. The performance of composite was evaluated by degradation of other persistent organic compounds, such as tartrazine (TA), janus green B (JGB), conggo red (CR), and caffeine (CF), also compared to other catalysts in literatures.

2. Materials and Methods

2.1 Materials

Dyes (99 %) were purchased from Sigma-Aldrich. Zinc nitrate hexahydrate ($(Zn(NO_3)_2.6H_2O$, 99 %), hexamethylenetetramine - HMTA ($C_6H_{12}N_4$, 99 %), urea ($(NH_2)_2CO$, 99 %), and sodium citrate ($Na_3C_6H_5O_7$, 99 %) were obtained from Merck. All of the reagents were used without any further purification.

2.2. Preparation of Nano ZnO

ZnO nanoparticles were simplified by precipitation method, without the hydrothermal process [22]. Typically, 0.1 mol $Zn(NO_3)_2.6H_2O$, 0.1 mol HMTA, and 0.01 mol sodium citrate were dissolved in a beaker containing 100 mL distilled water to form a clear solution. The mixed solution was heated up to 90 ^oC for 1 h. The precipitate was collected by filtering and washing with distilled water, and then dried at 80 ^oC overnight. Finally, nano ZnO was obtained by calcining the precipitate at 400 ^oC for 2 h at a heating rate of 1 ^oC/min via a furnace (Nabertherm, Germany, the max furnace temperature was 1200 ^oC).

2.3 Preparation of ZnO/g-C_3N_4 Composite

An exact amount of urea was finely crushed in an agate mortar prior to well mixing with 1 g of nano ZnO. The mixture was placed in a 100 mL crucible, covered with aluminum foil, and then placed in a furnace (Nabertherm, Germany, the max furnace temperature was 1200 ^oC). The temperature increased to 575 ^oC at a heating rate of 2 ^oC/min and the furnace remained at this temperature for 3 h. Finally, the sample was allowed to cool at room temperature and again finely ground to obtain the composite, which was denoted ZnO/g-C_3N_4 (1:*x*), where *x* is the mass of urea. For comparison, the pure g-C_3N_4 was also synthesized by the similar method to ZnO/g-C_3N_4, but without adding ZnO.

2.4 Characterization of Materials

The crystalline phase of the samples was investigated by X-ray powder Diffraction (Bruker D8 Ax, Germany). XRD patterns were obtained with Cu-Ka irradiation (40kV, 40 mA) at the 2θ ranging from 10 to 80 °. The FT-IR spectra were measured by Fourier transform infrared spectroscopy (FTIR, Madison, WI, USA). The morphology and size of samples were observed by a Transmission Electron Microscopy (TEM, JEM-JEOL 2100) and a Field Emission Scanning Electron Microscopy (FE-SEM, JEOL-7600F). The chemical composition of composite was determined by an Energy Dispersive Spectrometry (EDS: JEOL-Benelux). The textural properties were via N_2 adsorption/desorption isotherms using a micromeritics (Gemini VII). UV-vis diffuse reflectance spectra were measured on a UV-vis-NIR spectrometer Cary 500).

2.5 Photocatalytic Test

The photocatalytic activity of as-prepared samples was evaluated by the degradation of dyes in the water at room temperature under visible light irradiation (Hg lamp 250 W with the light source intensity of 16000 Lux). The lighting system was placed in a rectangular box with dimensions of 45×40×60 cm. The light was mounted on the ceiling of the box and the bottom had a magnetic stirrer. The system used two cooling fans placed symmetrically on both sides with a wind flow of 0.045 m^3/s. Typically, 50 mg of sample was added to 100 mL of 10 mg/L a dye in a 250 mL beaker. The distance from the lamp to the surface of the solution is 10 cm. The mixture was continuously stirred in the dark for 30 min to achieve adsorption-desorption equilibrium before irradiation. During the photoreaction, the sample was collected at a regular interval of 10 min and filtered by a syringe filter (0.45 µm PTFE membrane) to remove the catalyst. The dye concentration was analyzed by a spectrophotometer (DR 3900) at 663 nm. The degradation efficiency (*DE*), degradation capacity (*DC*), and rate constant of dye were calculated by the following equations:

$$DE\ (\%) = \frac{C_0 - C_t}{C_0} \times 100\% \tag{1}$$

$$DC\ (mg/g) = \frac{C_0 - C_t}{m} \times V \tag{2}$$

$$\ln\left(\frac{C_0}{C_t}\right) = k_{ap} \times t \tag{3}$$

where, k_{ap} (min^{-1}) is the rate constant, C_0 is the initial concentration of dye (mg/L), C_t is the concentration of dye in time (mg/L), *V* is the volume of dye solution (L), *m* is the mass of the catalyst (g), and *t* is the reaction time (min).

3. Results and Discussion

3.1 Characterization of the Catalyst

Figure 1 demonstrates the XRD patterns of ZnO, g-C_3N_4, and ZnO/g-C_3N_4 (1:4) samples. The diffraction peaks of (100), (002), (101), (102), (110), (103), (200), (112), (201), (004), and (202) planes were observed, which were well-indexed to the typical wurtzite hexagonal ZnO crystal structure (JCPDS No. 36–1451) [22]. Besides, no characteristic peak of any impurity detected confirmed the purity of ZnO, in Figure 1(a). This proved that HMTA and sodium citrate only acted as a precipitating and crystal orientation agents. The crystalline size (D) of as-prepared samples can be determined using the Scherrer formula [24] in Equation (4):

$$D = \frac{K\lambda}{\beta \cos\ \theta} \tag{4}$$

where, λ is the wavelength of the X-ray used (1.5406 Å), D is the crystallite size in the direction perpendicular to the lattice plane, β is the width (full-width at half-maximum, FWHM) of the X-ray diffraction peak in radians, θ is the Bragg angle, K is a numerical factor frequently referred to as the crystallite-shape factor. In addition to depending on the crystallite shape, the numerical factor K also depends on the definitions of the average crystallite size, where K = 0.9 is a good approximation. The crystalline sizes of the ZnO were calculate by planes in XRD pattern, the results are presented in Table 1. The average crystalline size of ZnO was 18.1 nm.

The g-C_3N_4 sample had two distinct diffraction peaks at 2θ of 13.0 and 27.6°, corresponding to the lattice planes (100) and (002), respectively, in Figure 1(b). It confirmed the structure of the crystalline g-C_3N_4 (JCPDS No. 87-1526) [25]. The strong peak at 27.6^o was a characteristic interlayer stacking of aromatic systems, indexed for graphitic materials. The d-spacing of lattice planes (d_{hkl}) can be determined based on Bragg's formula [26] in Equation (5):

$$d_{hkl} = \frac{n\lambda}{2\ \sin\ \theta} \tag{5}$$

As the result, the d_{hkl} was 0.323 nm, which was smaller than that of the crystalline g-C_3N_4 from the previous report [27]. The dense structure was likely due to the positioning of elec-

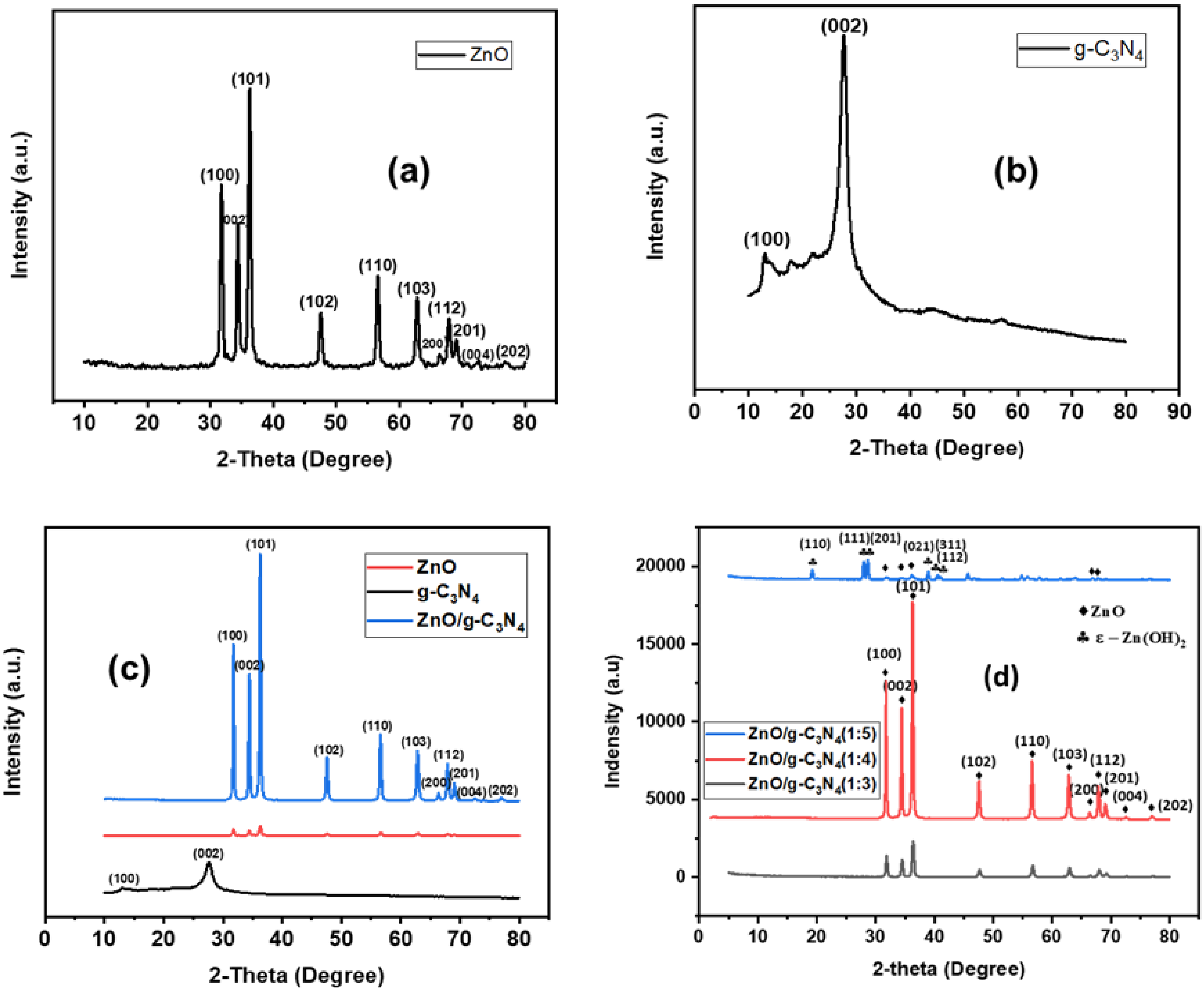

Figure 1. XRD patterns of the (a) ZnO, (b) g-C_3N_4, (c) combination of ZnO, g-C_3N_4, and ZnO/g-C_3N_4 (1:4), and (d) combination of g-C_3N_4/ZnO (1:x) composites

trons and the stronger bonding between the layers. The small-angle peak at 13.0° corresponded to a distance of 0.680 nm. This peak was presumably related to an in-plane structural packing motif, such as the hole-to-hole distance of the nitride pores in the crystalline. This distance was only slightly below the size of one tris-s-triazine unit (0.73 nm) [25]. The crystalline sizes size from (100) and (002) planes were 0.29 and 4.64 nm, average crystalline size off g-C_3N_4 was 2.46 nm, in Table 2.

As shown in Figure 1(c), the ZnO/g-C_3N_4 composite showed all characteristic peaks of pure ZnO but these peaks were much more intense than those of pure ZnO. While, the characteristic peaks of g-C_3N_4 did not appear, meaning a low crystallinity of g-C_3N_4 in the composite. Which might be assigned to the mechanical force during fine grinding, most of the g-C_3N_4 particles were evenly dispersed the composite. The crystalline size corresponding to each plane was increased from ZnO, the average crystalline size of ZnO/g-C_3N_4 was 29.14 nm (Table 3). This could be assigned to the sintering of urea after calcination at high temperature. The addition of ZnO in composite had little impact on the previous phase structure g-C_3N_4 but provided a more versatile strategy for hybrid structure manipulation. This can expect an improvement in catalytic activity.

The XRD patterns of other ZnO/g-C_3N_4 composites were analyzed and the results are presented in Figure 1(d). The XRD peaks of ZnO/g-C_3N_4 (1:3) and ZnO/g-C_3N_4 (1:5) had higher intensity than ZnO/g-C_3N_4 (1:4). In addition, the peaks corresponding to ε-$Zn(OH)_2$ were detected for the ZnO/g-C_3N_4 (1:5) samples. The average crystalline sizes of ZnO/g-C_3N_4 (1:3), ZnO/g-C_3N_4 (1:4), and ZnO/g-C_3N_4 (1:5) were 21.39, 27.00, and 22.76 nm, respectively. This proved that complete composite crystallites with a large size were produced at a certain ZnO/urea ratio.

The FE-SEM and EDS images of as-prepared samples are presented in Figure 2. The aggregate shape of ZnO was seen as clouds, they were assembled from ZnO nanoparticles with particle size approximately 20-30 nm, in Figure 2(a-b). The g-C_3N_4 material had a morphology as thin and curve flakes, their width was not uniform, but their thickness was about 20 nm, these flakes were gathered to form a porous structure, in Figure 2(c-d). The aggregated morphology of ZnO/g-C_3N_4 was relatively different from that of ZnO and C_3N_4. This might be due to the sintering process of urea in the presence of ZnO, resulting

Table 2. Crystalline size of C_3N_4 (*: average crystalline size)

Plane	Crystalline size (nm)
(100)	0.29
(002)	4.64
-	2.46*

Table 1. Crystalline size of ZnO (*: average crystalline size)

Plane	Crystalline size (nm)	Plane	Crystalline size (nm)
(100)	17.89	(200)	15.35
(002)	17.81	(112)	16.29
(101)	17.11	(201)	15.17
(102)	16.51	(004)	30.96
(110)	17.58	(202)	18.10
(103)	15.99	-	18.10*

Table 3. Crystalline size of ZnO/g-C_3N_4 (*: average crystalline size)

Plane	Crystalline size (nm)	Plane	Crystalline size (nm)
(100)	29.78	(200)	24.37
(002)	29.03	(112)	22.38
(101)	27.57	(201)	22.24
(102)	23.05	(004)	38.56
(110)	24.94	(202)	33.08
(103)	22.01	-	27.00*

in a clearer grain for composite instead of a flake. The aggregated size of the composite was about 5 µm consisting of ZnO and g-C_3N_4 nanoparticles with a smooth surface and a size of approximately 20-50 nm, in Figure 2(e-g). The EDS and element map results showed a uniform dispersion of the elements in composite despite the physical mixed calcination was used to prepare the sample. The EDS spectrum showed the atomic compositions of C, N, O, and Zn in the composite as 23.21, 14.67, 29.5 and 32.62 %, respectively.

The TEM results show that ZnO particles were clearly observed with the size of 20-30 nm, in Figure 3(a), which was highly consistent with the results of the XRD and SEM obtained above. Meanwhile, the ZnO/g-C_3N_4 composite showed spherical particles with the size of about 20-30 nm also the peanut particles with a length of about 80 nm and a width of about 40 nm, in Figure 3 (b-d). Which were corresponded to ZnO and g-C_3N_4 components, respectively, consisting in the composite.

The FT-IR spectra of samples are shown in Figure 4. For g-C_3N_4, several strong bands in the 1200-1650 cm^{-1} region were found to be stretching modes of −C−N− heterocycles. The well-resolved bands indicate a fairly high degree of ordering. The band at about 806 cm^{-1} could be attributed to the ring-sextant out-of-plane bending vibration characteristic of both triazine or heptazine ring systems [28-30]. The prominent absorption bands at 1202, 1225, and 1310 cm^{-1} were characteristic of the −C−NH−C− unit in *melam* [31-33], which is considered as the structural unit of g-C_3N_4 [31-33]. Therefore, a similar structural motif, corresponding to either trigonal C−N(−C)−C (full condensation) or bridging units C−NH−C (partial condensation), can be inferred for the polymer. Absorption found in the N−H stretching region between 3242 and 3088 cm^{-1} proves the presence of NH or NH_2 groups, which were most likely integral parts of the structure. For ZnO, the strong absorption peak at 3157 cm^{-1} could be due to the stretching of O−H modes of adsorbed H_2O. The presence peak at 1712 and 908 cm^{-1} in the higher frequency range indicates the prolonged O−H bond from the Zn−OH. The peak at 1383 cm^{-1} was described

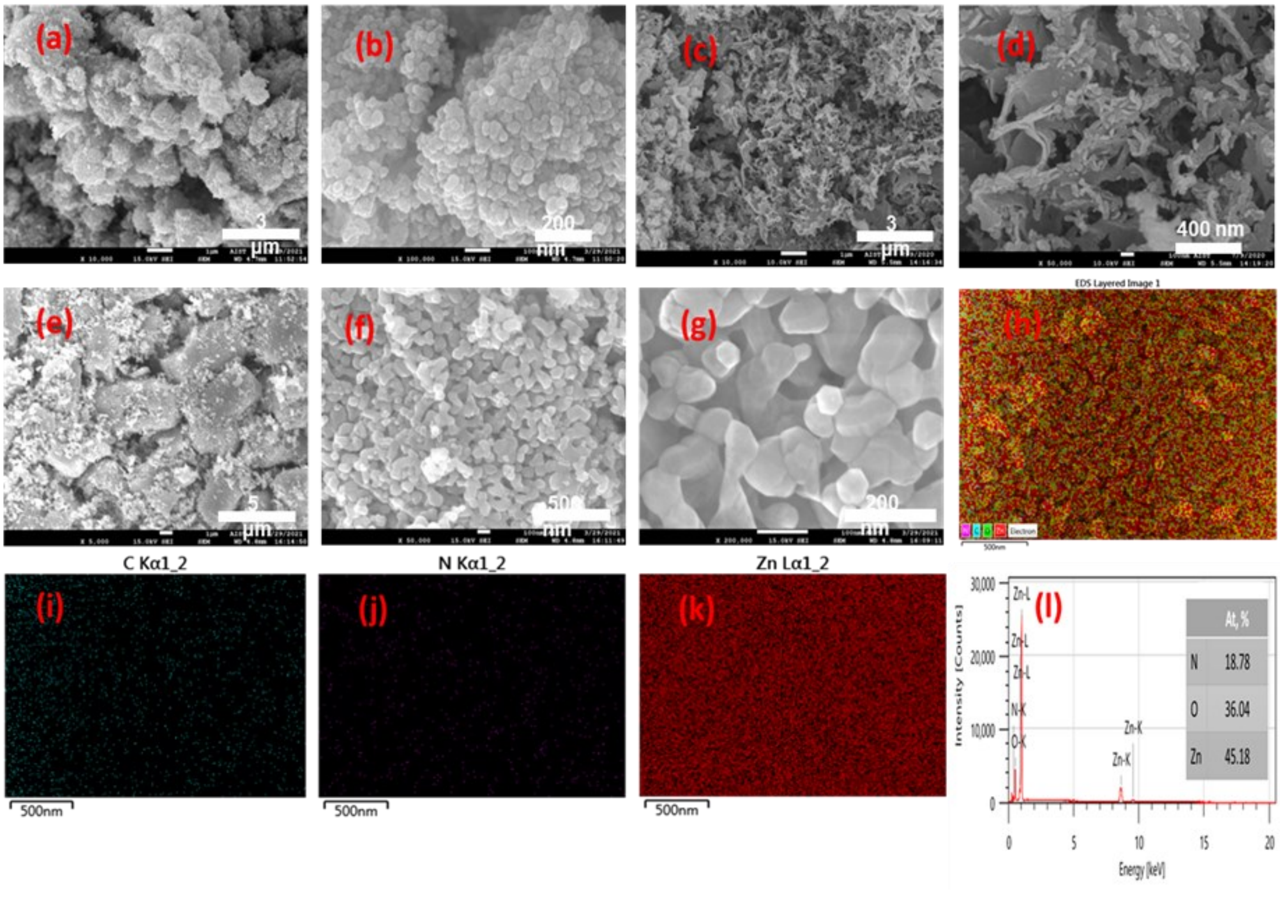

Figure 2. FE-SEM images of (a-b) ZnO, (c-d) g-C_3N_4, (e-g) ZnO/g-C_3N_4 (1:4) composite, (h) EDS image, (i) C elemental map, (j) N elemental map, (k) Zn elemental map, and (l) EDS spectrum of ZnO/g-C_3N_4 (1:4) composite

to be the stretching vibration of the nitrate (NO_3^-) band [34], while the intensive absorption band at 567 cm^{-1} was due to Zn−O stretching vibration [35]. The occurrence of the same peaks of ZnO and g-C_3N_4 in the ZnO/g-C_3N_4 sample confirmed the assembly of the composites but the intensity of the peaks became lower. Furthermore, the broadband peak of the g-C_3N_4 from 3242 to 3088 cm^{-1} was shifted towards the small wavenumber in the presence of ZnO. These changes indicated a strong surface interaction between components, quite than a simple physical mixture for composite. This was the cause of oscillations of Zn−C with the peaks at 1115 cm^{-1} appearing in the composite.

Figure 5 presents the N_2 adsorption / desorption isotherms and pore size distributions of the samples g-C_3N_4 and ZnO had type IV with H3 hysteresis loop, according to the IUPAC classification. The adsorption did not increase up to P/P_0 of 0.8 and the hysteresis loops approached P/P_0=1 indicating the presence of mesopore and macropore together in both samples. However, the hysteresis loop of ZnO was much lower than that of pure g-C_3N_4, showing a relative difference in their pore size distributions. As the results, the surface areas were 109.7 and 26.4 m^2/g and the pore volumes were 0.900 and 0.481 cm^3/g for C_3N_4 and ZnO, respectively, in Table 4. Meanwhile, the

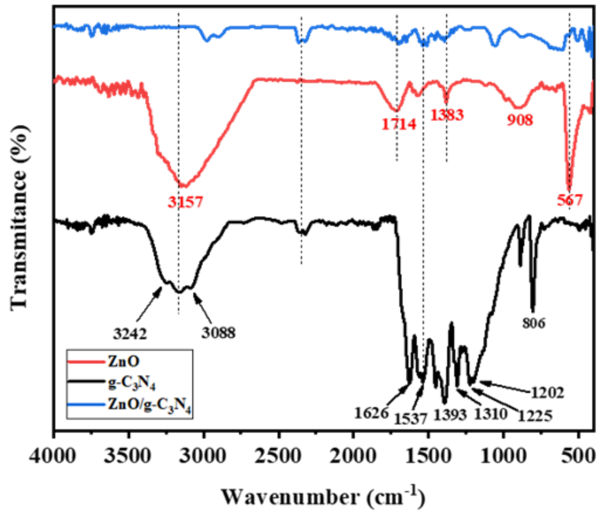

Figure 4. IR spectra of ZnO, g-C_3N_4, and ZnO/g-C_3N_4 (1:4) composite

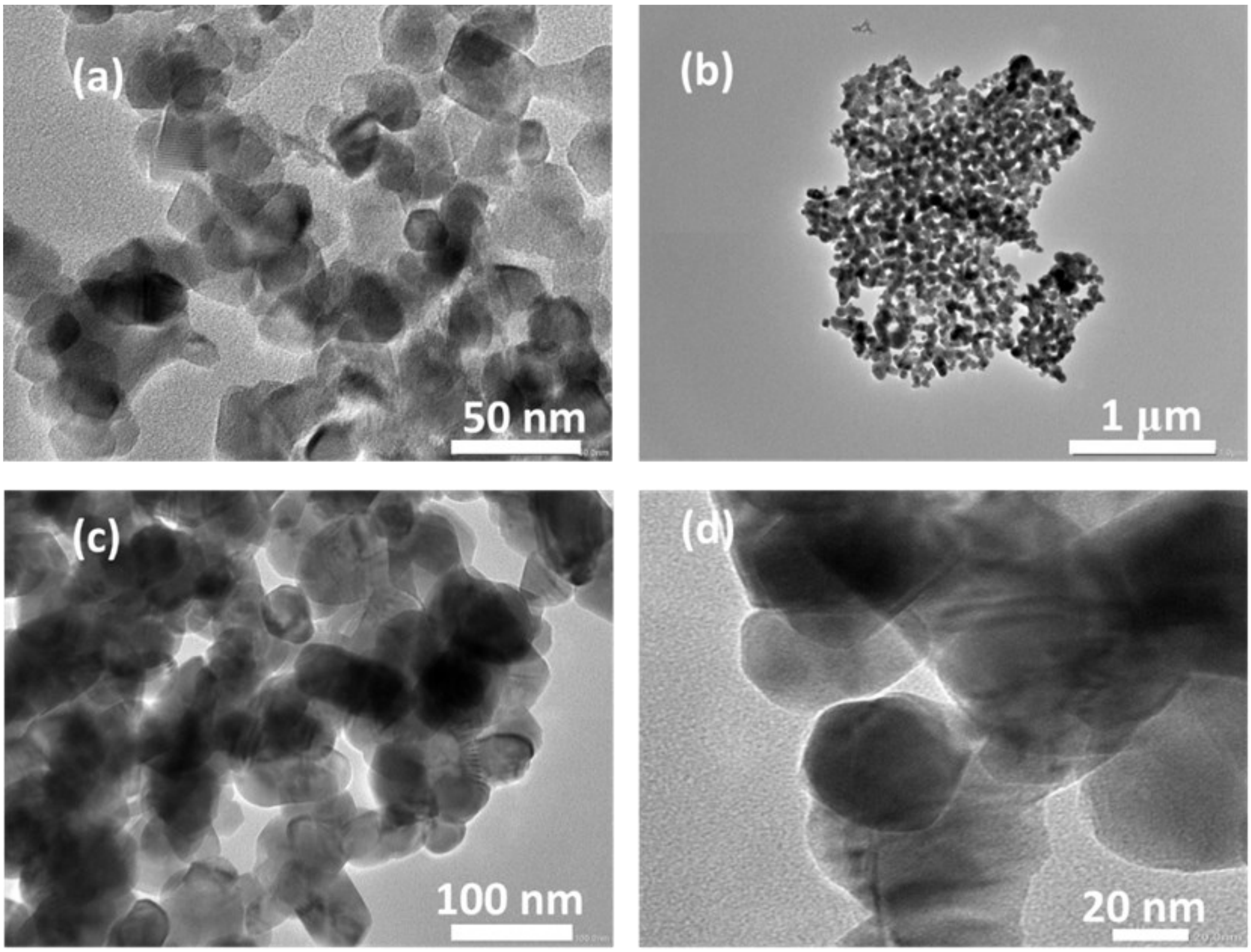

Figure 3. (a) TEM images of (a) ZnO and (b-d) ZnO/g-C_3N_4 (1:4) composite

$ZnO/g\text{-}C_3N_4$ nanocomposite seemed to have no hysteresis loop, implying a small pore volume. This was verified in the result of the pore size distribution, in Figure 5(b). The surface area, pore volume, and average pore size of the composite were 3.9 m^2/g, 0.034 cm^3/g, and 32.7 nm, respectively. Although as-prepared $g\text{-}C_3N_4$ exhibited a relatively high surface area, 11 times higher than normal $g\text{-}C_3N_4$ (~10 m^2/g) [36], it was sharply reduced for composite. This cause might come from the grinding process, the heating rate, or the sintering process of urea during the calcination.

Figure 6 shows the UV-Vis diffuse reflectance spectra and Tauc's plot of samples. The optical band gap values for all samples were determined by following equation [22]:

$$(\alpha h\nu)^2 = A(h\nu - E_g) \qquad (6)$$

where, h is Planck's constant, ν is the photon's frequency, α is the absorption coefficient, E_g is the band gap energy, and A is a proportionality constant. The $h\nu$ values were plotted against $(\alpha h\nu)^2$ and extended to calculate the E_g by Tauc's method. The samples all exhibited a light absorption in the range of 300-500 nm. The absorption curves of ZnO and $ZnO/g\text{-}C_3N_4$ were similar to each other with the steep absorption edge, they showed a quite different to $g\text{-}C_3N_4$. The characteristic features of Tauc

Table 4. The textural properties of $g\text{-}C_3N_4$, ZnO, and $ZnO/g\text{-}C_3N_4$ (1:4) composite

Sample	BET surface area (m^2/g)	Pore volume (cm^3/g)
ZnO	26.4	0.481
$g\text{-}C_3N_4$	109.7	0.900
$ZnO/g\text{-}C_3N_4$	3.9	0.034

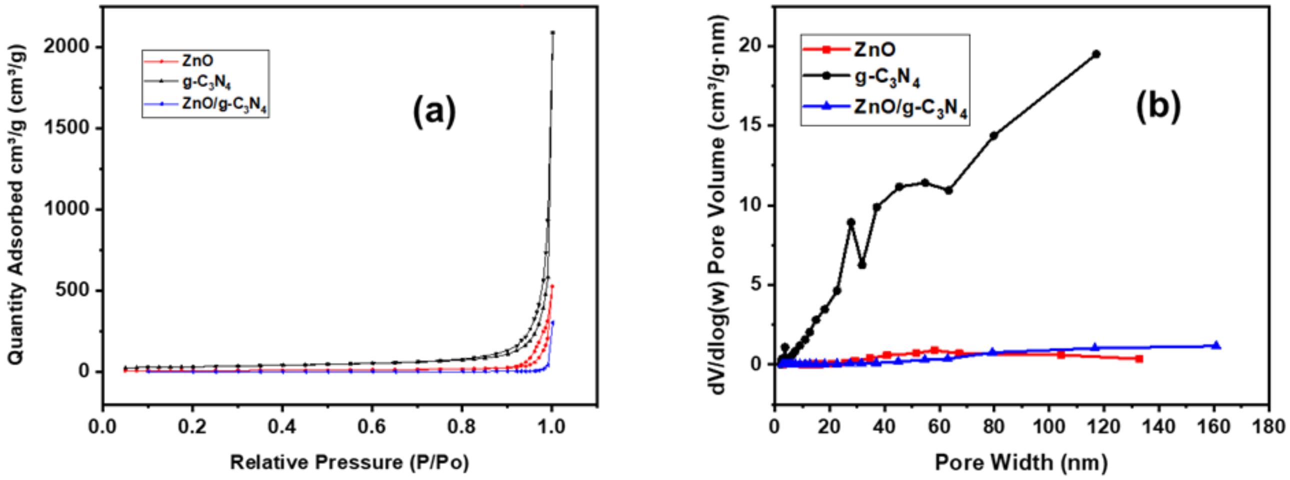

Figure 5. (a) N_2 adsorption/desorption isotherms and (b) pore size distributions of ZnO, $g\text{-}C_3N_4$, and $ZnO/g\text{-}C_3N_4$ (1:4) composite

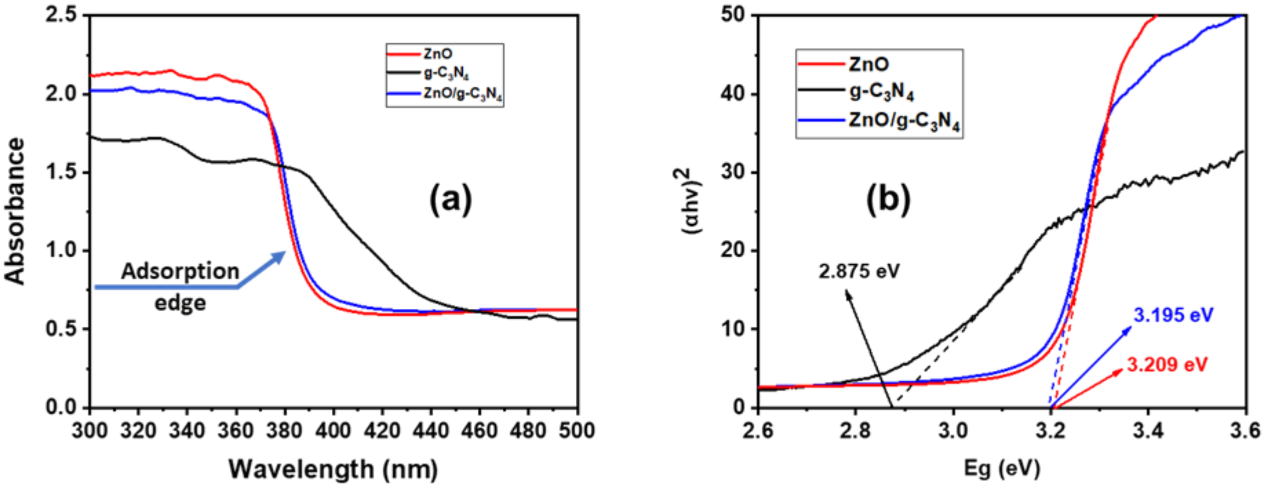

Figure 6. (a) UV-Vis diffuse reflectance spectra and (b) Tauc's plot of the as-synthesized samples

plots are evidence: at low photon energies the absorption approaches zero, the material is transparent; near the band gap value the absorption gets stronger and shows a region of linearity in this squared exponent plot. This linear region has been used to extrapolate to the X-axis intercept to find the band gap value. As the result, the E_g values of g-C_3N_4, ZnO, and ZnO/g-C_3N_4 composites were 2.875, 3.209, and 3.195 eV, respectively. The photocatalytic ability of a sample depends not only on the specific surface but also on many other parameters such as morphology, crystallinity, grain size, interface interaction, and the recombination of electron and hole [37,38].

3.2. Photodegradation Investigation

3.2.1. Effect of catalyst on degradation of MB

MB is one of the most frequently used. It is a water-soluble cationic dye and can reveal very harmful effects on living things such as difficulties in breathing, vomiting, diarrhea, nausea, and several negative impacts on the aquatic environment. MB is stable under UV-vis irradiation if there is no photocatalyst involved. In this investigation, the photocatalytic activities of ZnO, g-C_3N_4, and ZnO/g-C_3N_4 composite were evaluated by degrading MB at the remained reaction conditions (dosage catalyst of 0.5 g/L, MB concentration of 10 mg/L, and solution pH of 6.5), the results are shown in Figure 7. The g-C_3N_4 sample exhibits better adsorption than ZnO and ZnO/g-C_3N_4 composites, the large surface area and the high porous structure of g-C_3N_4, as presented in Table 4, can provide more active sites for adsorption of dye molecules. However, its photocatalyst ability was weaker, although its E_g was smaller than that of ZnO and ZnO/g-C_3N_4 composites. The *DE* values of MB in 90 min for ZnO, g-C_3N_4, and ZnO/g-C_3N_4 were 84.0, 76.0, and 93.2 %, respectively. These proved that the surface interaction of components in composite with the appearance of Zn−C bonds was the essential factor determining the catalytic ability of the composite rather than the surface area, pore volume, and band gap energy.

The *VB* and *CB* values of g-C_3N_4 and ZnO were calculated by the following equation [39]:

$$E_{CB} = \chi - E^c - 0.5E_g \quad (7)$$
$$E_{VB} = E_{CB} + E_g \quad (8)$$

where, χ is the absolute electronegativity of the atom semiconductor, expressed as the geometric mean of the absolute electronegativity of the constituent atoms, which is defined as the arithmetic mean of the atomic electron affinity and the first ionization energy. The values of χ were 4.725 eV [40] and 5.790 eV [41] for g-C_3N_4 and ZnO, respectively; E^c is the energy of free electrons of the hydrogen scale (4.500 eV); E_g is the band gap of the semiconductor; E_{CB} is the conduction band potential, and E_{VB} is the valence band potential.

The values of E_g, E_{CB}, and E_{VB} of the the ZnO and g-C_3N_4 samples are shown in Table 5. The significant improvement of photocatalytic degradation of MB in the composite is illustrated schematically in Figure 8. Due to a wide band gap energy (3.209 eV), under visible light, pure ZnO itself cannot excite electrons from the valence band (*VB*) to the conduction band

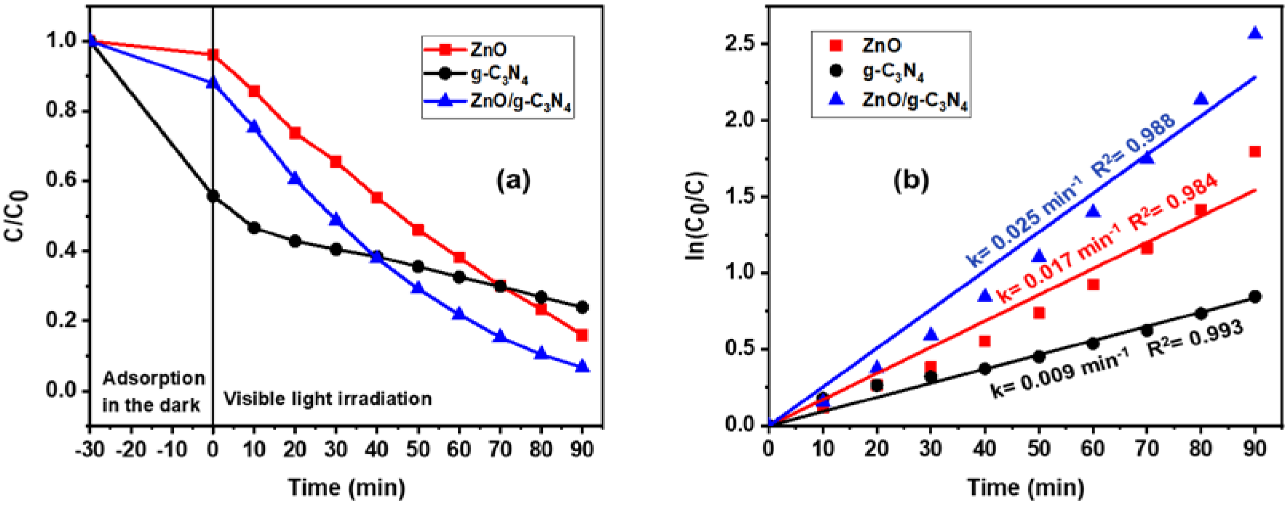

Figure 7. (a) Degradation of MB in ZnO, g-C_3N_4, and ZnO/g-C_3N_4 (1:4) composite under visible light, and (b) fitting plots of the first-order kinetic model in Equation (3). The reaction conditions: dosage catalyst of 0.5 g/L, MB concentration of 10 mg/L, pH = 6.5).

(*CB*). ZnO excitation is possible only with ultraviolet irradiation whose radiant energy is equal to or greater than it is band gap energy. While the g-C_3N_4 in the composite system can be excited by visible light as its excitation energy falls in the visible spectrum. Due to the well-established interface between the organic and metal oxide (graphitic carbon nitride and zinc oxide), photoinduced electrons can be migrated from the *CB* of g-C_3N_4 to the *CB* of ZnO. Concomitantly, the holes in the *VB* of ZnO could transfer to the *VB* of g-C_3N_4. The movement of photoinduced electron and hole are quite reasonable because the conduction band edge potential of g-C_3N_4 is more negative than that of ZnO and the valence band potential of ZnO is more positive than g-C_3N_4 [42].

The *VB* value of g-C_3N_4 lay between the *VB* and *CB* values of ZnO, and the *CB* value of ZnO lay between the *VB* and *CB* values of g-C_3N_4. That could make the recombination process of $e^- - h^+$ in ZnO/g-C_3N_4 materials to be slower than that of the component materials. The delayed recombination of photoinduced electron-hole for better dye degradation efficiency. The diagram reactions were revealed the following:

$$\mathrm{ZnO/g\text{-}C_3N_4} + h\nu \rightarrow \mathrm{ZnO/g\text{-}C_3N_4}\ (e^- + h^+) \quad (9)$$
$$e^- + O_2 \rightarrow {}^{\cdot}O_2^- \quad (10)$$
$${}^{\cdot}O_2^- + H^+ \rightarrow HO_2^{\cdot} \quad (11)$$
$$HO_2^{\cdot} + HO_2^{\cdot} \rightarrow H_2O_2 + O_2 \quad (12)$$
$$H_2O_2 + h\nu \rightarrow 2{}^{\cdot}OH \quad (13)$$
$$h^+ + H_2O \rightarrow OH^{\cdot} + H^+ \quad (14)$$
$$h^+ + OH^- \rightarrow OH^{\cdot} \quad (15)$$
$$O_2^{\cdot -}/OH^{\cdot} + MB \rightarrow \text{intermediate products} \quad (16)$$
$$O_2^{\cdot -}/OH^{\cdot} + \text{intermediate products} \rightarrow \ldots\ CO_2 + H_2O + \text{salts} \quad (17)$$

In this study, the E_g values of ZnO and ZnO/g-C_3N_4 were close, the surface area of ZnO/g-C_3N_4 was lower than those of ZnO and g-C_3N_4 (in Table 4). However, the catalytic ability of the ZnO/g-C_3N_4 composite was higher than that of ZnO and g-C_3N_4. The large crystalline size and the surface interaction between ZnO and g-C_3N_4, along with the difference of their *VB* and *CB* energy levels, resulted in reduced recombination of electron-hole were the causes of enhanced photocatalytic performance of the ZnO/g-C_3N_4 composite [37,38].

Table 5. The values of E_g, E_{CB}, and E_{VB} of the the ZnO and g-C_3N_4 samples

Sample	E_g (eV)	E_{CB} (eV)	E_{VB} (eV)
ZnO	3.209	- 0.315	2.894
g-C_3N_4	2.875	- 1.213	1.662

Table 6. Comparison of degradation of MB by various materials

Catalyst	Reaction conditions	Observation	Reference
Cu-doped TiO_2/ZnO	[Cat.]=1.5 g/L, [MB]=20 mg/L, pH = 7.5-8, under visible light irradiation	73.2 % of MB was removed in 120 min	[44]
Ag-ZnO/GO	[Cat.] = 1.0 g/L, [MB]= 15 mg/L, pH =8.5-9.0, under visible light irradiation	58.0 % of MB was removed in 90 min	[45]
Ni-doped $ZnFe_2O_4$ nanoparticles	[Cat.] = 0.3 g/L, [MB]= 20 mg/L, pH =3, under UV-Vis (λ=365 nm) light irradiation	94 % of MB was removed in 90 min	[46]
$AgTi_5$	[Cat.] = 1.0 g/L, [MB]= 8 mg/L, pH =6.5, under UV light irradiation	97.1 % of MB was removed in 200 min	[47]
ZnO nanoparticles	[Cat.]=0.5 g/L, [MB]=10 mg/L, pH = 6.5, under visible light irradiation	84.0 % of MB was removed in 90 min, degradation capacity of 17 mg/g	This work
g-C_3N_4	[Cat.]=0.5 g/L, [MB]=10 mg/L, pH = 6.5, under visible light irradiation	76.0 % of MB was removed in 90 min, degradation capacity of 15 mg/g	This work
ZnO/g-C_3N_4 composite	[Cat.]=0.5 g/L, [MB]=10 mg/L, pH = 6.5, under visible light irradiation	93.2 % of MB was removed in 90 min, degradation capacity of 19 mg/g	This work

3.2.2. Effect of mass ratio on the degradation of MB

The effect of the ZnO/urea ratio on the efficiency of the composite is shown in Figure 9. The results showed that at 1:3 and 1:5 ratios, composites gave slower reaction rates than ZnO. The rate constants of ZnO, ZnO/g-C_3N_4 (1:3), and ZnO/g-C_3N_4 (1:5) were 0.017, 0.009, and 0.011 min^{-1}, respectively. The composite sample at the 1:4 ratio had the highest efficiency among as-prepared composites, the *DE* value was 93.2 % and the rate constant was 0.025 min^{-1}. Since the band gap energy had a small effect on catalytic activity, as mentioned above, the crystalline size, which was mentioned in Section 3.1, could be a decisive factor in proving the degradation efficiency of the ZnO/g-C_3N_4 composite.

3.2.3. Effect of catalyst dosage on the degradation of MB

The experiments were carried out by employing different catalyst dosages (0.25, 0.5, 0.75, and 1.0 g/L) and other conditions remained. The reaction rate increased for increasing in dosage catalyst, in Figure 10. As the result, the *DE* value increased to 71.2 and 97.2 %, and the rate constant increased from 0.012, 0.025, 0.028, and 0.031 min^{-1}, however, the *DC* was decreased from 28.5 to 9.7 mg/g when the catalyst dosage increased from 0.25 to 1.0 g/L, respectively.

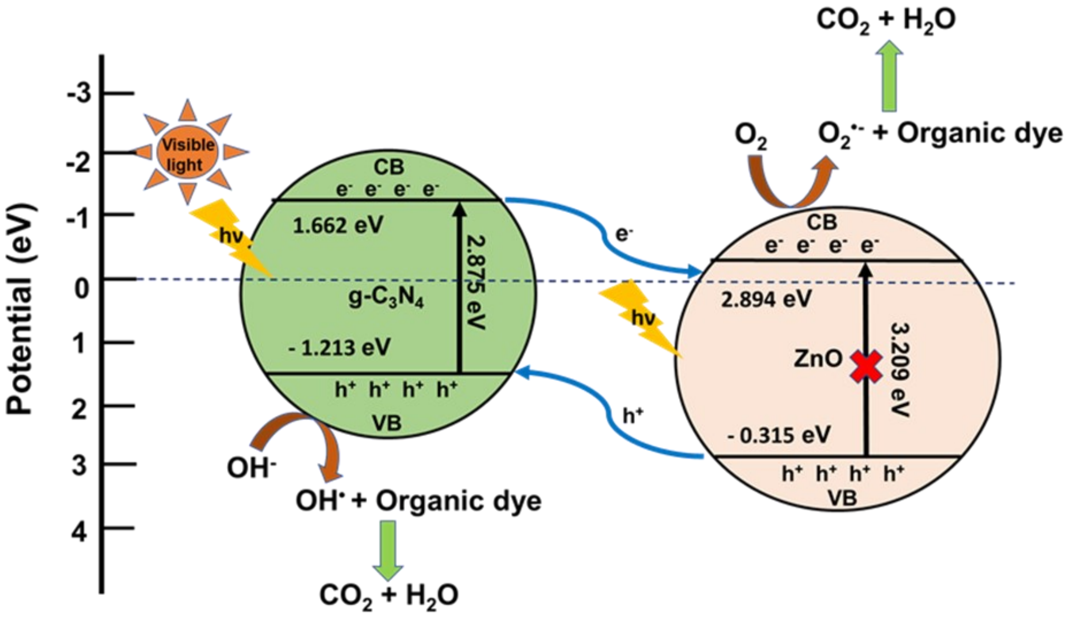

Figure 8. Photocatalytic mechanism of MB in nanocomposite under visible light

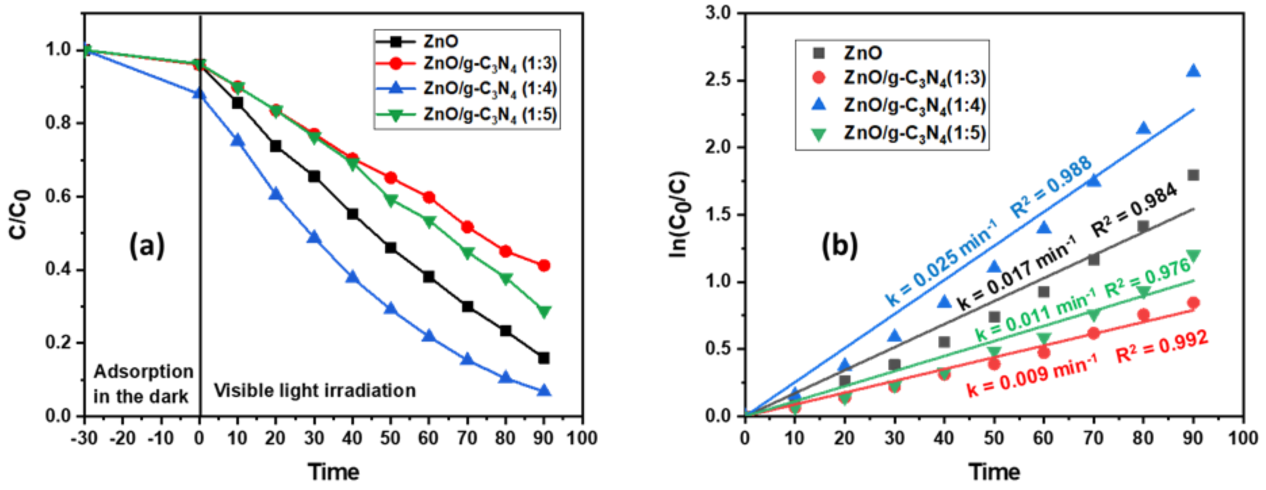

Figure 9. (a) Effect of ZnO/Urea mass ratio on the photocatalysis efficiency of MB, (b) fitting plots (3). The reaction conditions: MB concentration of 10 mg/L and pH = 6.5

Increasing the catalyst dosage led to an increase in the number of active sites on the catalyst surface and the density of the catalyst particles in the illuminated region [43]. However, this resulted in a reduced MB degradation per gram of the catalyst, as shown in Figure 10(c). This result might come from the increased amount of catalyst suspended in the solution, short wave-tailed photons could not enter the reaction mixture, reducing the penetration of other visible light particles and increasing the scattering effect. Furthermore, when more catalysts were added, each catalyst had less chance of contact with MB molecules because the reaction was fast as shown in Figure 10(a). As a result, the efficiency and reaction rate could be improved with increasing catalyst dosage, but the degradation capacity became lower.

3.2.4. Effect of dye concentration on the degradation of MB

The concentration of MB varied from 5 to 20 mg/L while other conditions remained. In Figure 11 (a), the *DE* value and rate constant were significantly decreased for increasing the MB concentration. The *DE* at 90 min and the reaction rate were 98.6 % and 0.040 min^{-1}, respectively, at the 5 mg/L, these were reduced to 28.3 % and 0.003 min^{-1}, respectively, at 20 mg/L. However, the results showed that *DC* reached the maximum at 10 mg/L.

The negative effect of increased mount MB on reaction can be interpreted by the following reasons: (1) The number of MB molecules, adsorbed on the active sites of the catalyst surface, increases with the initial concentration of MB dye. Therefore, the generation rate of $O_2^\bullet$ and $OH^\bullet$ radicals on the same active sites became decreased; (2) Alternatively, increasing the dye concentration leads to generating a large number of intermediates from dye molecules along with the reaction, and may compete with MB molecules in the constant total active sites; (3) Otherwise, with an increase in the initial dye concentration, the solution becomes more intensely colored and the path length of photons by the catalyst decreases, and consequently the degradation rate is reduced [15]. Despite lowering in degradation efficiency and reaction rate of MB with increasing the initial concentration of dye, the degradation capacity at 10 mg/L during 90 min (18.6 mg/g) was higher than that of other concentrations of MB

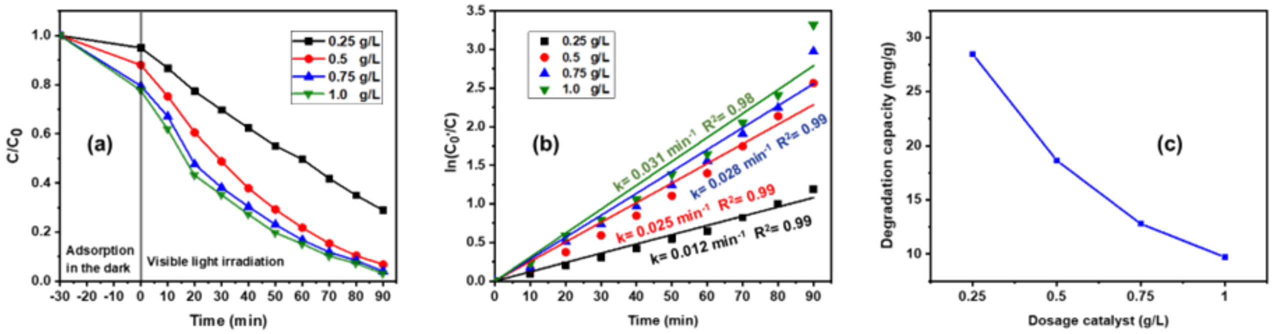

Figure 10. (a) Effect of catalyst dosage on degradation of MB, (b) fitting plots (3), and (c) degradation capacity versus dosage catalyst. The reaction conditions: MB concentration of 10 mg/L and pH = 6.5

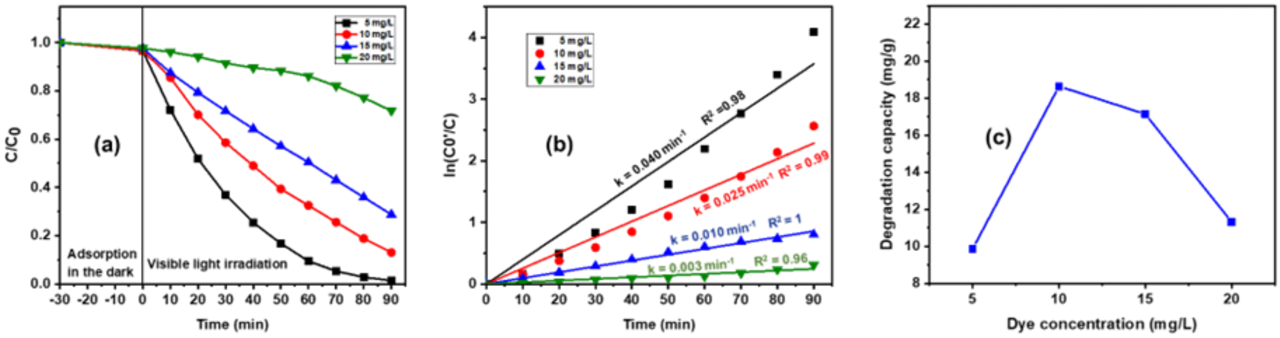

Figure 11 (a) Effect of initial dye concentration on degradation of MB, (b) fitting plots (3), and (c) degradation capacity versus MB concentration. The reaction conditions: Dosage catalyst of 0.5 g/L and pH= 6.5

(Figure 11c). Furthermore, it was expected that the degradation efficiency could be achieved to 100 % regardless of initial concentrations if the reaction time was elongated as shown in Figure 11 (a).

3.2.5. Effect of solution pH on degradation of MB

In the design process for wastewater treatment, the solution pH will play a decisive role. Not only catalyst surface and wastewater composition but structure and ionization of functional groups are also affected by solution pH. For research on the effect of solution pH on degradation of MB, it was varied from 4.0 to 10.0 under the fixed other conditions. We can see that the degradation rate of MB was significantly affected by pH. The reaction rate at pH 4.0 was the slowest, it increased when the solution pH increased to 6.5 and it was decreased when the pH further increased to 8.0. However, at the pH value of 11.0, the degradation efficiency and rate constant reached the maximum at 100 % and 0.055 min^{-1}, respectively, in Figure 12. These proved that the relatively high alkaline environment could accelerate the photocatalytic reaction of composites. This could be explained that the high pH values could facilitate more OH- ions to be reacted with h^+ to form OH• radicals, thereby improving the dye degradation efficiency. However, a high pH environment also increased the solubility of ZnO, which led to a decrease in the stability and reusability of the catalyst. Therefore, pH = 6.5 was a suitable medium for the degradation of dyes in water.

The point of zero charge (pH_{pzc}) of the ZnO/g-C_3N_4 (1:4) sample was measured by the pH drift method. Initially, a 250 mL beaker containing 100 mL of 10 mg/L MB solution was adjusted to the pH solution values from 2 to 11 by HCl 0.1 M or NaOH 0.1 M solutions. Next, 0.05 g of ZnO/g-C_3N_4 sample was poured into the beaker and stirred for 24 h at room temperature, then the final pH (pH_{final}) value was measured. The plot of pH_{final} versus $pH_{initial}$ will intersect the $pH_{initial}$ line at a point where it was defined as the pH_{pzc} of the catalyst.

The point of zero charge (pH_{pzc}) is an important parameter affecting the adsorption capacity of materials for organic substances. The pH_{pzc} is defined as the pH of the solution at which the charge of the positive surface sites is equal to the charge of the negative sites, the adsorbent surface charge is zero. The surface charge is negative at pH > pH_{pzc} and positive at pH < pH_{pzc}. Figure 13 shows the pH_{pzc} value of ZnO/g-C_3N_4 determined by the pH deviation method. The obtained pH_{pzc} value was 7.7. This was completely consistent with the pH survey results presented in Figure 12 [43]. At pH lower than 6.5, the surface of the catalyst was positively charged due to the adsorption of H^+ ion, which respelled the MB cation dyes and the

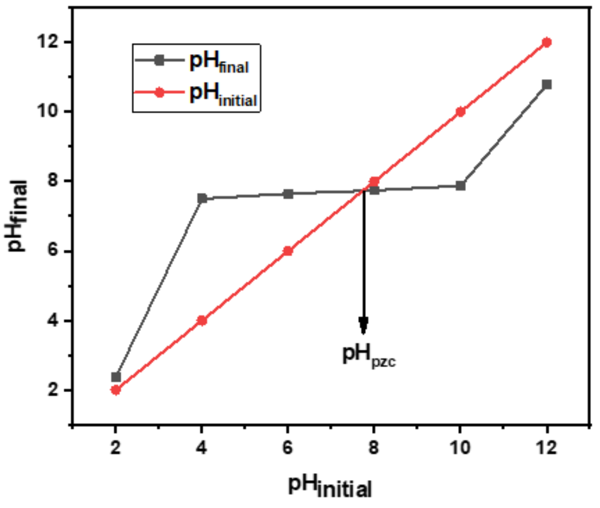

Figure 13. Determination of the point of zero charge (pH_{pzc}) of the ZnO/g-C_3N_4 (1:4) sample

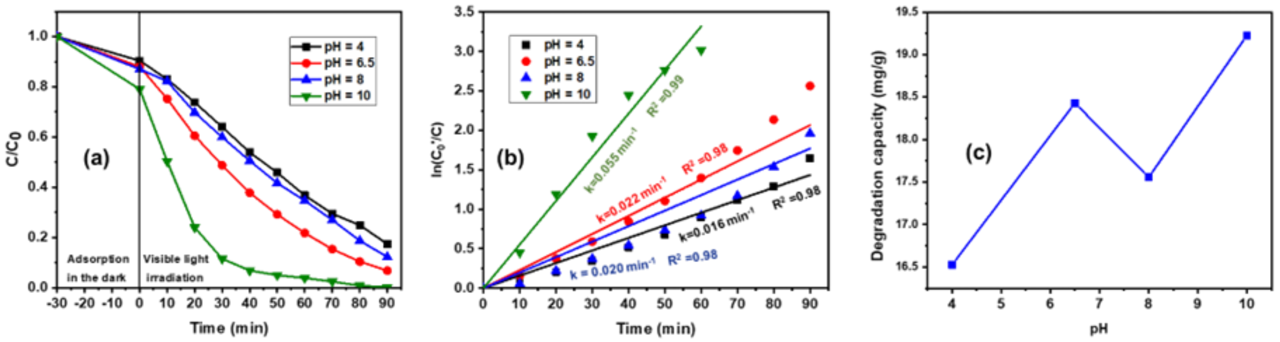

Figure 12. (a) Effect of pH solution on degradation of MB, (b) fitting plots, and (c) degradation capacity at different pH values. The reaction conditions: dosage catalyst of 0.5 g/L and MB concentration of 10 mg/L

degradation process was decreased. Meanwhile, at pH above 7.7, the surface of the composite was negative charge, while MB was a cationic dye. As the result, the improvement of the adsorption between MB on surface of composite could enhance the degradation process. When the pH of the solution was higher than pH_{pzc}, where the surface of the ZnO particles could be negatively charged by absorbing OH- ions, it interfered with the adsorption of MB, however, the enhancement of the formation process of •OH radicals remained dominant, which resulted in increasing the catalytic efficiency at high pH values.

3.2.6. Degradation of various pollutants and comparison with other catalysts

The as-synthesized ZnO/g-C_3N_4 (1:4) composite was tested with other organic compounds (tartrazine, janus green B, conggo red, and caffeine) under the same conditions (0.5 g/L, dyes concentration of 10 mg/L, solution pH = 6.5). The adsorption and decomposition of conggo red were the greatest, *DE* reached 100% in 10 min and the rate constant reached 0.239 min^{-1}, which were in intermediate speeds for the janus green B, methylene blue, and tartrazine dyes. The caffeine was the most difficult to degrade, the *DE* and rate constant were 34 % and 0.005 min^{-1}, respectively, in Figure 14.

Table 6 shows a brief comparison of MB removal efficiency by different catalysts through photocatalytic activity. The directed comparison of the ZnO/g-C_3N_4 composite with other catalysts is challenging since each study evaluated the removal capacity under different conditions. But, the relative performance of the ZnO/g-C_3N_4 composite can be evaluated indirectly. It could be observed that under the condition of visible light, ZnO/g-C_3N_4 composite had a better degradation efficiency in a shorter reaction time than Cu-doped TiO_2/ZnO [44] and Ag-ZnO_d/GO [45]. In the case of using the UV-light for reaction, the degradation efficiency of the composite was slightly lower than that of Ni-doped $ZnFe_2O_4$ [46] and $AgTi_5$ [47]. However, Ni-doped $ZnFe_2O_4$ nanoparticles need a relatively acidic medium of pH 3.0 and $AgTi_5$ took 2.2 times longer for degradation of MB than ZnO/g-C_3N_4, in Table 6. Therefore, the ZnO/g-C_3N_4 nanocomposite prepared by the facile method using popular material urea was expected to be a cheap and environmentally friendly catalyst for large-scale applications.

4. Conclusions

ZnO nanoparticles, the crystal size of 18.1 nm, were successfully fabricated by the facile precipitation method. The degradation efficiency in 90 min and rate constant of ZnO for MB degradation were 84.0 % and 0.017 min^{-1}, respectively. The g-C_3N_4 sample showed a high surface area and pore volume of 109.7 m^2/g and 0.481 cm^3/g, and a small crystal size of 2.46 nm. The interplanar distance of aromatic units of g-C_3N_4 was 0.323 nm. As the result, g-C_3N_4 exhibited high adsorption capacity, but low photocatalytic activity for MB. Its degradation efficiency and rate constant were 76.0 % and 0.009 min^{-1}, respectively. The ZnO/g-C_3N_4 composites with different mass ratios were successfully synthesized by the physical mixing-calcination method. At the ratio 1:4, the ZnO/g-C_3N_4 composite had the strongest photo-

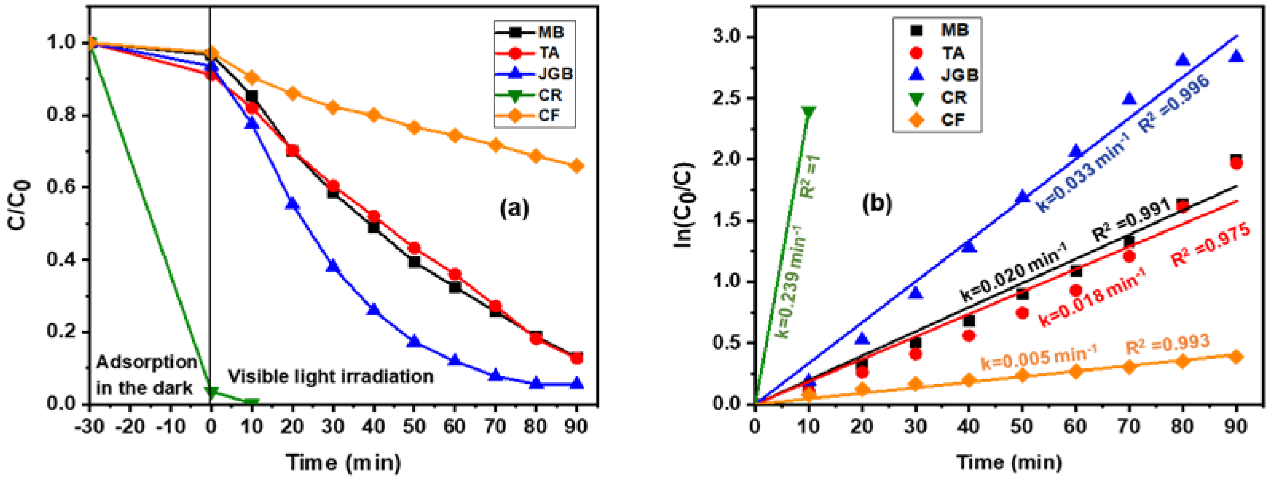

Figure 14. (a) The degradation of other organic dyes on composite, and (b) fitting plots (3). The reaction conditions: dosage catalyst of 0.5 g/L, dye concentration of 10 mg/L and pH = 6.5

catalytic reaction for MB among the studied ratios. This composite had a smaller surface area and pore volume compared to g-C_3N_4 and even ZnO. Its E_g was slightly smaller than that of ZnO. The results of the study showed that there was surface interaction between the components, which was revealed by oscillations of Zn−C bonds. As the result, the ZnO/g-C_3N_4 composite displayed a superior photoreaction. This proves that the surface interaction between ZnO and g-C_3N_4, which benefited the rapid transport of photoinduced charge carriers, was a decisive factor for the photocatalytic efficiency of the composite. Besides, ZnO/g-C_3N_4 was also shown to be an efficient photocatalyst towards other persistent organic substances, such as TA, JGB, CR, and CAF, showing the degradation efficiency and the reaction rate of 100 % in 40 min and 0.239 min^{-1} for CR. Moreover, the photocatalytic efficiency of the composite was also compared with the catalysts in the literature. These results indicated the high potential application of composite in the removal of toxic organic compounds in wastewater.

Acknowledgments

The authors are grateful for the financial support Vietnam National Foundation for Science and Technology Development (NAFOSTED) under grant number 104.05-2018.333.

References

[1] Pereira, L., Alves, M. (2012). Dyes—environmental impact and remediation. In *Environmental protection strategies for sustainable development*. Dordrecht: Springer.

[2] Dixit, S., Yadav, A., Dwivedi, P. D., Das, M. (2015). Toxic hazards of leather industry and technologies to combat threat: a review. *Journal of Cleaner Production*, 87, 39-49. DOI: 10.1016/j.jclepro.2014.10.017

[3] Gallidabino, M., Weyermann, C., Marquis, R. (2011). Differentiation of blue ballpoint pen inks by positive and negative mode LDI-MS. *Forensic Science International*, 204 (1), 169-178. DOI: 10.1016/j.forsciint.2010.05.027

[4] Guerra, E., Llompart, M., Garcia-Jares, C. (2018). Analysis of dyes in cosmetics: challenges and recent developments. *Cosmetics*, 5 (3), 47. DOI: 10.3390/cosmetics5030047

[5] Oplatowska-Stachowiak, M., Elliott, C.T. (2017). Food colors: Existing and emerging food safety concerns. *Critical Reviews in Food Science and Nutrition*, 57 (3), 524-548. DOI: 10.1080/10408398.2014.889652

[6] Wainwright, M. (2011). 6 - Dyes for the medical industry. In M. Clark (Ed.), *Handbook of Textile and Industrial Dyeing*. Cambridge: Woodhead Publishing.

[7] Ali, H. (2010). Biodegradation of synthetic dyes - a review. *Water, Air, & Soil Pollution*, 213 (1), 251-273. DOI: 10.1007/s11270-010-0382-4

[8] Ardila-Leal, L.D., Poutou-Piñales, R.A., Pedroza-Rodríguez, A.M., Quevedo-Hidalgo, B.E. (2021). A Brief History of Colour, the Environmental Impact of Synthetic Dyes and Removal by Using Laccases. *Molecules*, 26 (13). DOI: 10.3390/molecules26133813

[9] Kannan, N., Sundaram, M.M. (2001). Kinetics and mechanism of removal of methylene blue by adsorption on various carbons—a comparative study. *Dyes and Pigments*, 51 (1), 25-40. DOI: 10.1016/S0143-7208(01)00056-0

[10] Sarioglu, M., Atay, U. (2006). Removal of methylene blue by using biosolid. *Global Nest J.*, 8(2), 113-120. DOI: 10.30955/gnj.000351

[11] Obotey Ezugbe, E., Rathilal, S. (2020). Membrane Technologies in Wastewater Treatment: A Review. *Membranes*, 10(5), 89. DOI: 10.3390/membranes10050089

[12] Karcher, S., Kornmüller, A., Jekel, M. (2002). Anion exchange resins for removal of reactive dyes from textile wastewaters. *Water Research*, 36 (19), 4717-4724. DOI: 10.1016/S0043-1354(02)00195-1

[13] Ennigrou, D.J., Gzara, L., Romdhane, M.R. B., Dhahbi, M. (2009). Cadmium removal from aqueous solutions by polyelectrolyte enhanced ultrafiltration. *Desalination*, 246 (1-3), 363-369. DOI: 10.1016/j.desal.2008.04.053

[14] Verma, A.K., Dash, R.R., Bhunia, P. (2012). A review on chemical coagulation/flocculation technologies for removal of colour from textile wastewaters. *Journal of Environmental Management*, 93 (1), 154-168. DOI: 10.1016/j.jenvman.2011.09.012

[15] Vu, A.-T., Xuan, T.N., Lee, C.-H. (2019). Preparation of mesoporous $Fe_2O_3 \cdot SiO_2$ composite from rice husk as an efficient heterogeneous Fenton-like catalyst for degradation of organic dyes. *Journal of Water Process Engineering*, 28, 169-180. DOI: 10.1016/j.jwpe.2019.01.019

[16] Sivakumar, A., Murugesan, B., Loganathan, A., Sivakumar, P. (2014). A review on decolourisation of dyes by photodegradation using various bismuth catalysts. *Journal of the Taiwan Institute of Chemical Engineers*, 45 (5), 2300-2306. DOI: 10.1016/j.jtice.2014.07.003

[17] Fu, J., Yu, J., Jiang, C., Cheng, B. (2018). g-C_3N_4-Based heterostructure photocatalysts. *Advanced Energy Materials*, 8 (3), 1701503. DOI: 10.1002/aenm.201701503

[18] Fan, M., Li, T., Li, G., Ma, H., Zhao, S., Yang, K., Kränkel, C. (2017). Graphitic C_3N_4 as a new saturable absorber for the mid-infrared spectral range. *Optics Letters*, 42(2), 286-289. DOI: 10.1364/OL.42.000286

[19] Wang, X., Maeda, K., Thomas, A., Takanabe, K., Xin, G., Carlsson, J.M., Domen, K., Antonietti, M. (2009). A metal-free polymeric photocatalyst for hydrogen production from water under visible light. *Nature Materials*, 8 (1), 76-80. DOI: 10.1038/nmat2317

[20] Wang, Y., Wang, X., Antonietti, M. (2012). Polymeric graphitic carbon nitride as a heterogeneous organocatalyst: from photochemistry to multipurpose catalysis to sustainable chemistry. *Angewandte Chemie International Edition*, 51 (1), 68-89. DOI: 10.1002/anie.201101182

[21] Bhatia, S., Verma, N. (2017). Photocatalytic activity of ZnO nanoparticles with optimization of defects. *Materials Research Bulletin*, 95, 468-476. DOI: 10.1016/j.materresbull.2017.08.019

[22] Vu Anh, T., Pham, T.A.T., Mac, V.H., Nguyen, T.H. (2021). Facile Controlling of the Physical Properties of Zinc Oxide and Its Application to Enhanced Photocatalysis. *Journal of Analytical Methods in Chemistry*, 2021, 5533734. DOI: 10.1155/2021/5533734

[23] Lee, P.J., Saion, E., Al-Hada, N.M., Soltani, N. (2015). A Simple Up-Scalable Thermal Treatment Method for Synthesis of ZnO Nanoparticles. *Metals*, 5 (4). DOI: 10.3390/met5042383

[24] Pham, T.A.T., Tran, V.A., Le, V.D., Nguyen, M.V., Truong, D.D., Do, X.T., Vu, A.-T. (2020). Facile Preparation of ZnO Nanoparticles and Ag/ZnO Nanocomposite and Their Photocatalytic Activities under Visible Light. *International Journal of Photoenergy*, 2020, 8897667. DOI: 10.1155/2020/8897667

[25] Thomas, A., Fischer, A., Goettmann, F., Antonietti, M., Müller, J.-O., Schlögl, R., Carlsson, J.M. (2008). Graphitic carbon nitride materials: variation of structure and morphology and their use as metal-free catalysts. *Journal of Materials Chemistry*, 18 (41), 4893-4908. DOI: 10.1039/B800274F

[26] De Graef, M., McHenry, M.E. (2012). Structure of materials: an introduction to crystallography, diffraction and symmetry. New York: Cambridge University Press.

[27] Bojdys, M.J., Müller, J.O., Antonietti, M., Thomas, A. (2008). Ionothermal synthesis of crystalline, condensed, graphitic carbon nitride. *Chemistry–A European Journal*, 14 (27), 8177-8182. DOI: 10.1002/chem.200800190

[28] Blagden, N. (2001). Crystal engineering of polymorph appearance: the case of sulphathiazole. *Powder Technology*, 121 (1), 46-52. DOI: 10.1016/S0032-5910(01)00373-4

[29] Tiekink, E.R., Vittal, J.J. (2006). *Frontiers in Crystal Engineering*. Iowa: John Wiley & Sons.

[30] Yarger, J.L., Wolf, G.H. (2004). Polymorphism in liquids. *Science*, 306 (5697), 820-821. DOI: 10.1126/science.1104417

[31] Jansen, M., Jäschke, B., Jäschke, T. (2002). Amorphous multinary ceramics in the Si-BNC system. *High Performance Non-Oxide Ceramics I*, 137-191. DOI: 10.1007/3-540-45613-9_3

[32] Senker, J., Rössler, E. (2001). Triphenyl phosphite: a candidate for liquid polyamorphism. *Chemical Geology*, 174 (1-3), 143-156. DOI: 10.1016/S0009-2541(00)00313-2

[33] Tarjus, G., Kivelson, S.A., Nussinov, Z., Viot, P. (2005). The frustration-based approach of supercooled liquids and the glass transition: a review and critical assessment. *Journal of Physics: Condensed Matter*, 17 (50), R1143. DOI: 10.1088/0953-8984/17/50/R01

[34] Lee, P.J., Saion, E., Al-Hada, N.M., Soltani, N. (2015). A simple up-scalable thermal treatment method for synthesis of ZnO nanoparticles. *Metals*, 5 (4), 2383-2392. DOI: 10.3390/met5042383

[35] Bouzid, H., Faisal, M., Harraz, F.A., Al-Sayari, S.A., Ismail, A.A. (2015). Synthesis of mesoporous Ag/ZnO nanocrystals with enhanced photocatalytic activity. *Catalysis Today*, 252, 20-26. DOI: 10.1016/j.cattod.2014.10.011

[36] Han, Q., Wang, B., Gao, J., Cheng, Z., Zhao, Y., Zhang, Z., Qu, L. (2016). Atomically thin mesoporous nanomesh of graphitic C3N4 for high-efficiency photocatalytic hydrogen evolution. *ACS Nano*, 10 (2), 2745-2751. DOI: 10.1021/acsnano.5b07831

[37] Kumar, S., Kumar, A., Kumar, A., Balaji, R., Krishnan, V. (2018). Highly Efficient Visible Light Active 2D-2D Nanocomposites of N-ZnO-g-C_3N_4 for Photocatalytic Degradation of Diverse Industrial Pollutants. *ChemistrySelect*, 3 (6), 1919-1932. DOI: 10.1002/slct.201703156

[38] Yang, Z., Yan, J., Lian, J., Xu, H., She, X., Li, H. (2016). g-C_3N_4/TiO_2 Nanocomposites for Degradation of Ciprofloxacin under Visible Light Irradiation. *ChemistrySelect*, 1 (18), 5679-5685. DOI: 10.1002/slct.201600861

[39] Gao, J., Zhou, Y., Li, Z., Yan, S., Wang, N., Zou, Z. (2012). High-yield synthesis of millimetre-long, semiconducting carbon nitride nanotubes with intense photoluminescence emission and reproducible photoconductivity. *Nanoscale*, 4 (12), 3687-3692. DOI: 10.1039/C2NR30777D

[40] Wu, J., Xie, Y., Ling, Y., Dong, Y., Li, J., Li, S., Zhao, J. (2019). Synthesis of flower-like g-C_3N_4/BiOBr and enhancement of the activity for the degradation of bisphenol A under visible light irradiation. *Frontiers in Chemistry*, 649. DOI: 10.3389/fchem.2019.00649

[41] Xu, Y., Schoonen, M.A.A. (2000). The absolute energy positions of conduction and valence bands of selected semiconducting minerals. *American Mineralogist*, 85(3-4), 543-556. DOI: 10.2138/am-2000-0416

[42] Wang, Y., Shi, R., Lin, J., Zhu, Y. (2011). Enhancement of photocurrent and photocatalytic activity of ZnO hybridized with graphite-like C_3N_4. *Energy & Environmental Science*, 4 (8), 2922-2929. DOI: 10.1039/C0EE00825G

[43] Kragović, M., Stojmenović, M., Petrović, J., Loredo, J., Pašalić, S., Nedeljković, A., Ristović, I. (2019). Influence of Alginate Encapsulation on Point of Zero Charge (pHpzc) and Thermodynamic Properties of the Natural and Fe(III) - Modified Zeolite. *Procedia Manufacturing*, 32, 286-293. DOI: 10.1016/j.promfg.2019.02.216

[44] Khaki, M.R.D., Shafeeyan, M.S., Raman, A.A.A., Daud, W.M.A.W. (2018). Evaluating the efficiency of nano-sized Cu doped TiO_2/ZnO photocatalyst under visible light irradiation. *Journal of Molecular Liquids*, 258, 354-365. DOI: 10.1016/j.molliq.2017.11.030

[45] Tran Thi, V.H., Pham, T.N., Pham, T.T., Le, M.C. (2019). Synergistic adsorption and photocatalytic activity under visible irradiation using Ag-ZnO/GO nanoparticles derived at low temperature. *Journal of Chemistry*, 2019. DOI: 10.1155/2019/2979517

[46] Padmapriya, G., Manikandan, A., Krishnasamy, V., Jaganathan, S.K., Antony, S.A. (2016). Spinel $Ni_xZn_{1-x}Fe_2O_4$ ($0.0 \leq x \leq 1.0$) nano-photocatalysts: synthesis, characterization and photocatalytic degradation of methylene blue dye. *Journal of Molecular Structure*, 1119, 39-47. DOI: 10.1016/j.molstruc.2016.04.049

[47] Messih, M.A., Ahmed, M., Soltan, A., Anis, S.S. (2017). Facile approach for homogeneous dispersion of metallic silver nanoparticles on the surface of mesoporous titania for photocatalytic degradation of methylene blue and indigo carmine dyes. *Journal of Photochemistry and Photobiology A: Chemistry*, 335, 40-51. DOI: 10.1016/j.jphotochem.2016.11.001